TOUCHLESS ELECTROSTATIC DETUMBLE OF A REPRESENTATIVE BOX-AND-PANEL SPACECRAFT CONFIGURATION

Trevor Bennett[(1)] **and Hanspeter Schaub**[(2)]

[(1)]*Graduate Research Assistant and NSTRF Fellow, Ann and H.J Smead Department of Aerospace Engineering Sciences, University of Colorado. Email: Trevor.Bennett@Colorado.edu*

[(2)]*Alfred T. and Betty E. Look Professor of Engineering, Associate Chair of Graduate Affairs, Ann and H.J Smead Department of Aerospace Engineering Sciences, University of Colorado, 431 UCB, Colorado Center for Astrodynamics Research, Boulder, CO 80309-0431. Email: hanspeter.schaub@Colorado.edu*

ABSTRACT

Active debris removal mission concepts seek to directly alleviate the growing on-orbit congestion as more sustainable space mission practices are introduced. Further, servicing missions may reduce the number of space assets that become debris. The most challenging aspect of active debris removal and servicing missions is the debris capture, or mechanical interface, with the target object. Observed targets range in tumble rates from fractions of a degree per second to tens of degrees per second. Many debris capture techniques, such as robotic manipulators, require or benefit from low tumble rates and pose an increased collision risk. Methods such as nets or harpoons have traded the complexity of capturing a tumbling object with the complexity of controlling a tethered pair of orbital objects. Electrostatic detumble is a touchless servicer concept that amplifies the natural on-orbit charging of spacecraft to reduce the target's tumble rate. This work extends the electrostatic detumble approach to a more generic spacecraft geometry. This work develops the electrostatic detumble control law and demonstrates the performance through numerical simulations of a box-and-panel spacecraft analogue.

Keywords: Touchless detumble, active debris removal, contactless, electrostatic actuation, satellite servicing, formation flying.

1. INTRODUCTION

The large asset values of Geostationary orbit (GEO) satellites and the significant demand for GEO orbit slots are prime motivations for developing on-orbit servicing and active debris removal (ADR) strategies for this region. In a recent report, the collection of GEO satellites was insured for over 13 Billion US dollars.[11] Furthermore, the small magnitude of clearing perturbations, such as atmospheric drag in low-Earth orbits (LEO), leads to natural decay times on the order of centuries. The strict satellite

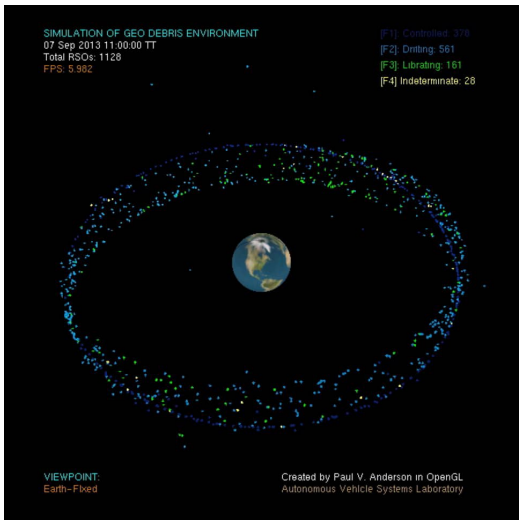

Figure 1. GEO debris population as seen in the Earth-fixed frame.[1]

end-of-life practices ensure that uncontrolled satellites and objects are relocated; forestalling a disintegration of currently viable orbits.[1] However, without active debris or defunct satellite removal strategies, it is predicted currently viable orbits will become too congested to be used in the near future.[1] The congestion in GEO, visible in Figure 1, is growing where over 700 objects meter-sized or larger are uncontrolled. The extreme scenario of this trend is best captured by the Kessler Syndrome where the on-orbit population is sufficiently dense that a single conjunction event will trigger a domino effect disintegration of orbit objects in similar orbits. In addition, removing a few key debris objects could drastically reduce the collision risks, reduce fuel expenditure for collision avoidance, and extend the operational life for satellites in the prized GEO belt.[1] Active debris removal and on-orbit servicing space mission concepts that require an active servicing vehicle to approach and mechanically interface with a defunct satellite or target object.[12,40] Establishing a mechanical interface provides the opportunity for robotic interaction, such as refueling operations, and

more-simple servicer control during the larger debris removal and re-orbiting ΔV maneuvers. For example, the Defense Advanced Research Projects Agency (DARPA) Phoenix approach extends the value of on-orbit assets by harvesting satellite components to re-build the target or transfer to another spacecraft.[25] A currently unavailable yet required critical capability is the ability to efficiently grapple large tumbling orbital objects. Electrostatic detumble is a touchless method of reducing the tumble rate of target object prior to any further proximity operations or mechanical capture.

Electrostatic actuation of spacecraft has been explored as early as the 1960s since developing both the understanding of charging dynamics and electrostatic control for Earth-orbiting satellites.[20,3,34,38,39,26,33] In addition, electrostatic actuation with a passive object is being considered for both large GEO debris mitigation[31,24,23,15] as well as touchless asteroid spin control.[22,21] Specifically, Reference[10] shows that the Geosynchronous Orbit environment is a favorable candidate region where space plasma conditions enable electrostatic interaction across 10's to 100's of meters requiring only Watt-levels of power. Electrostatic interaction performs best with lower density and higher electron and ion temperatures as seen in GEO compared to lower Earth orbits. The electrostatic detumble mission concept, as shown in Figure 2, requires a servicing craft to modulate charge transfer via an electron or ion gun such that a differential electrostatic detumble torque is generated. Reference[35] first introduced how electrostatic charging can be controlled to apply torques on a spinning debris object without requiring physical contact as shown in Figure 2. Such electrostatic actuation with a passive object has been used as an Electrostatic Tractor (ET), and is further considered for both large GEO debris removal[31,24,23] and orbit corrections or re-orbit target objects.[16,15]

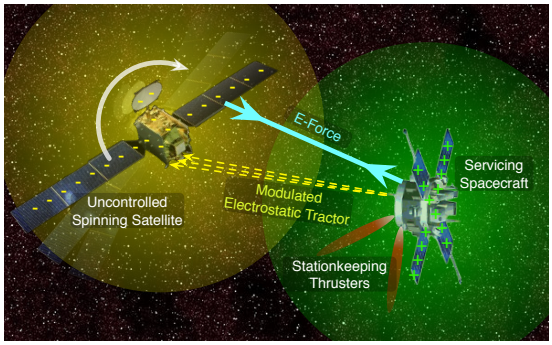

Figure 2. Electrostatic actuation technology enabling diverse service mission profiles

Electrostatic actuation was first applied to reducing the one-dimensional rotation of a cylindrical target using a spherical servicer at a fixed relative position.[35] The electrostatic forces and torques were modeled using the Multi-Sphere Method[36] (MSM) and a Lyapunov control was developed using an analytical approximation of the torque. This approach was numerically validated through simulation and a 1-dimensional rotation terrestrial experiment.[37] This concept was expanded to account for 3-dimensional cylinder tumbles again relying on analytical approximations of the MSM torque.[7] The 3-dimensional analysis demonstrated that a Lyapunov control approach was able to account for deep-space and on-orbit detumble performance prediction for nominal, tugging, and pushing servicer activity.[4] Furthermore, optimization of the servicer relative position increased the detumble controllability and decreased detumble time.[5] Note in all previous 1-dimensional and 3-dimensional electrostatic detumble studies, the target is assumed to be axisymmetric and the charge center and mass center are coincident.

The focus of this work is to apply the electrostatic detumble concept to more generic spacecraft geometries by removing the charge center and axisymmetric assumptions. Reference 17 demonstrated that an offset between the mass center and charge center for the cylindrical target produces significant variations in the electrostatic torque. These variations are not well captured by the analytical expressions used in the detumbling Lyapunov control developments to date rendering the previous approaches insufficient for variations in mass center location. This motivates a control approach that can account for non-coincident mass and charge centers. In addition, recent advances in attaining the MSM model for generic spacecraft geometries allows for study of geometries beyond the previously used cylindrical, or axisymmetric, target.[18] More generic spacecraft geometries are characterized by three distinct principal inertias. A new electrostatic detumble control is required that does not rely on the symmetry arguments and analytical torque approximations used by the axisymmetric studies. Proposed is the use of a Lyapunov optimal control that leverages the MSM model to not make assumptions on the target geometry nor require analytical torque expressions. Of interest is how reduced the MSM model can be to reduce to computational effort of an on-board control implementation.

The recently launched GOES-R spacecraft provides a suitable spacecraft geometry to inform a generic spacecraft analogue. The generic spacecraft considered in this work is a box-and-panel spacecraft that concentrates most of the satellite mass in a central cubic bus with a large solar array connected to a top edge of the bus. This manuscript introduces the Multi-Sphere Method (MSM) used to model generic spacecraft geometries. Also described are the Linearized Relative Orbit Elements that are used for relative motion guidance and control. This work develops a Lyapunov optimal detumble control using the MSM model of the spacecraft and demonstrates the performance through numerical simulations.

2. ELECTROSTATIC MODELING

The electrostatic interaction between two craft is accurately approximated for faster than real time control and simulation applications by the The Multi-Sphere Method (MSM). MSM represents the spacecraft electrostatic charging model as a collection of spherical conduc-

tors carefully dispersed through the body.[36] Consider the well-studied cylinder object shown in Figure 3 which is electrostatically manipulated by the collection of electrostatic forces induced by the presence of a charged spherical servicer spacecraft. The particular MSM configuration is generated by matching the force, torque, and capacitance outputs[36] or by electric field matching[18] of the commercial software package Maxwell for a variety of attitudes and ranges.

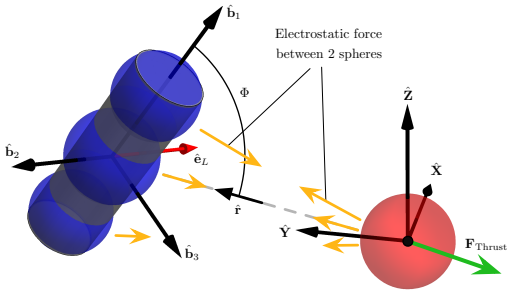

Figure 3. 3 sphere MSM cylinder and spherical spacecraft configuration.[7]

2.1. Forces and Torques from the Multi-Sphere Method

The MSM model is used in faster-than-real-time simulations and control developments where the sphere-to-sphere electrostatic forces are determined by the charges residing on each sphere shown in Figure 3. The time-varying charges are computed from the prescribed electric potentials,ϕ_i , according to the self and mutual capacitance relationships in (1), where $k_c = 8.99 \times 10^9$ N·m^2/C^2 and q_i is the charge of each sphere.[32,29]

$$\phi_i = k_c \frac{q_i}{R_i} + \sum_{j=1, j\neq i}^{m} k_c \frac{q_j}{r_{i,j}} \tag{1}$$

The term R_i denotes the radius of the i^{th} conducting sphere and $r_{i,j}$ denotes the vector between the i^{th} and j^{th} conducting spheres. These relations can be collected in matrix form where a, b, c are the cylinder spheres' centers.

$$\begin{bmatrix} \phi_1 \\ \phi_2 \\ \vdots \\ \phi_2 \\ \phi_2 \end{bmatrix} = k_c [E] \begin{bmatrix} q_1 \\ q_{2,1} \\ \vdots \\ q_{2,n-1} \\ q_{2,n} \end{bmatrix} \tag{2}$$

$$[E] = \underbrace{\begin{bmatrix} 1/R_1 & 1/r_{1,1} & 1/r_{1,2} & \cdots & 1/r_{1,n} \\ 1/r_{1,1} & 1/R_{2,1} & 1/l_{1,2} & \cdots & 1/l_{2,n} \\ \vdots & \vdots & \ddots & & \vdots \\ 1/r_{n-1,1} & 1/l_{n-1,1} & \cdots & 1/R_{2,n-1} & 1/l_{n-1,n} \\ 1/r_{n,1} & 1/l_{n,1} & \cdots & 1/l_{n,n-1} & 1/R_{2,n} \end{bmatrix}}_{\text{Elastance}} \tag{3}$$

The sphere charges, q_i for a particular configuration, or time step, are achieved by solving (2) with known electrostatic potentials, ϕ_i. The forces and torques on the cylinder are computed by inserting the resulting sphere charges, q_i, and separation to the target mass center, r_i, into the summations

$$\boldsymbol{F}_2 = k_c q_1 \sum_{i=1}^{n} \frac{q_{2,i}}{r_{1,i}^3} \boldsymbol{r}_{1,i} \tag{4a}$$

$$\boldsymbol{L}_2 = k_c q_1 \sum_{i=1}^{n} \frac{q_{2,i}}{r_{1,i}^3} \boldsymbol{r}_{1,i} \times \boldsymbol{r}_i \tag{4b}$$

(4b) provides the full MSM torque expression. However, the square matrix used to compute the charge has size equivalent to the number of MSM spheres and introduces a position-dependent coupling of the control potential ϕ to the sphere charges q_i. The numerical simulations use a full MSM model where an analytic approximation of the MSM torque was formerly utilized in the control developments.[35,4]

2.2. Modeling the Generic Box and Panel Geometry

Consider a more generic spacecraft design with similarities to the GOES-R Earth-observing satellite. Similar to the cylindrical target case, the box-and-panel spacecraft is electrostatically manipulated by a spherical servicer spacecraft. The box-and-panel spacecraft geometric properties in Table 1 dictates a center-to-center separation distance of 17.5 meters for the servicer to remain at 3-4 target craft radii. The box-and-panel spacecraft with

Table 1. Geometric parameters for box and panel detumble system.

Parameter	Value	Description
r	17.5 m	Servicer-target separation
s	3 m	Bus/Panel Side Length
l	8.5 m	Length of the Panel
h	0.2 m	Thickness of Panel

two and three sphere MSM distributions is shown in Figure 4(a) and 4(b), respectively.[18]

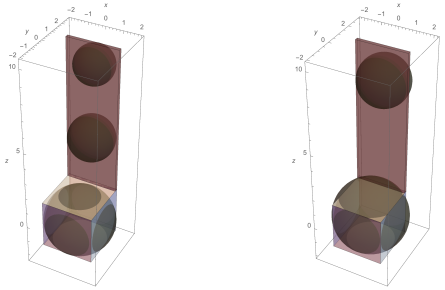

(a) Three sphere (b) Two sphere

Figure 4. Distributions of MSM spheres for the box and panel.

The box-and-panel uses 3000 kg for the dry mass of the spacecraft which is an analogue for the GEOS-R spacecraft. The panel thickness selected by Reference 18 is assumed to have the maximum solar panel density of 100 grams per cubic centimeter.[14] The mass of the spacecraft bus is computed from the dry mass less the solar panel mass. The center of mass is computed relative to the center of the cubic spacecraft bus where the z-axis is aligned with the long axis of the panel, the x-axis is normal to the top face of the solar panel, and the y-axis completes a right-handed system. The most conservative electrostatic detumble performance demonstration occurs with a maximum spacecraft inertia computed using the highest density solar panel. Decreased solar panel density ill improve detumble performance because an equivalent electrostatic torque drives a greater reduction in the tumble rate. This work explores the sensitivity to mass and inertia by allowing a 1000 kilogram mass to assume different static positions within the spacecraft bus. Using the properties in Table 2, the computed inertia matrix for the box-and-panel spacecraft with the offset mass centered in the spacecraft bus is

Table 2. Mass parameters for box and panel detumble system.

Description	Value	Units
Solar panel density	100	g/cm^3
Mass of solar panel	510	kg
Mass of bus	1490	kg
Offset mass	1000	kg
Spacecraft CM	[0, 0.238, 0.9775]	m
Offset mass shift	[1.5, 0.0, 0.0]	m
Alt. Spacecraft CM	[0.5, 0.238, 0.9775]	m

$$I_{\text{BaP}} = \begin{bmatrix} 21632.3 & 0 & 0 \\ 0 & 21183.5 & -3407.57 \\ 0 & -3407.57 & 4948.87 \end{bmatrix} \quad (5)$$

Allowing the spacecraft offset mass to reside at the positive x-axis edge of the bus shifts the center-of-mass along the positive x-axis by 0.5 meters and drives the alternative spacecraft inertia to be

$$I_{\text{BaP}} = \begin{bmatrix} 20132.3 & 357.0 & 1466.25 \\ 357.0 & 21183.5 & -3407.57 \\ 1466.25 & -3407.57 & 4948.87 \end{bmatrix} \quad (6)$$

Several MSM configurations of the box-and-panel spacecraft are considered. Of interest is the electrostatic detumble sensitivity to MSM model complexity for generic target objects. This research question is addressed by reducing the complexity, and thereby fidelity, of the target MSM model. Three configurations are selected: three-sphere, two-sphere, and a single effective sphere.[18] Table 3 details the location of each sphere measured from the spacecraft bus center.

Table 3. Center of mass location with respect to MSM locations.

Sphere	Radius, [m]	Location
R_c	2.039490	[0, -0.008373, -0.166258]
R_s	1.323119	[0, 1.318888, 4.583897]
R_p	1.120085	[0, 1.554560, 8.971854]
R_c	2.202207	[0, 0.134982, 0.209640]
R_p	1.467764	[0, 1.596384, 8.182859]
R_c	3.021	[0, 0.626, 2.914]

3. MORE GENERAL DETUMBLE TARGET CONSIDERATIONS

Several considerations are required for more generic geometries to avoid errors in torque modeling, such as incorrect sign, which drive growth in the target tumble rate. The center of mass location may not coincide with the electrostatic charge center. Knowing the target mass center offset is critical to modeling the electrostatic detumble torque. Also of interest is the viability of the analytical torque approximation approach for generic target geometries which is employed for axisymmetric targets. These considerations are central to formulating a generic geometry electrostatic detumble control scheme.

3.1. Cylindrical Target Center of Mass Offsets

Consider the case where the center of mass is does not coincide with the center of the geometry as has been assumed for the cylinder target shown in Figure 3 to this point.[4] This reasonable scenario, exemplified by an empty upper stage and mass concentrations around the rocket nozzle bell, introduces the possibility that the Multi-Sphere Model or analytical torque approximation used for the particular target may have asymmetric torque characteristics as a function of rotation rate. Reference 4 demonstrated how a $g(\Phi) = \gamma \sin(2\Phi)$ was sufficient for correctly capturing torque sign and magnitude of the 3-sphere model cylinder. Furthermore, the $g(\Phi)$ invoked

symmetry in the Lyapunov control proof to guarantee detumble stability. In the presence of a mass offset, a new $g(\Phi)$ is computed by empirically matching the output torque of a 3-sphere model with mass offset to the terms in Eq. (7).

$$f(\theta) = a_0 + a_1\cos(\Phi) + b_1\sin(\Phi) + a_2\cos(2\Phi) + b_2\sin(2\Phi) \tag{7}$$

The resulting fit in Eq. (8) is for the 3-sphere cylinder with a mass offset of x along the slender axis and projection angle Φ.

$$f(\Phi) = (p_1 x)\cos(\Phi) + (p_2 x^2 + p_3)\sin(2\Phi) \tag{8}$$

The terms p_i are specifically fit for a servicer spacecraft effective sphere radius. This form agrees closely with the Appropriate Fidelity Models (AFMs) derived by Reference 17. The AFMs derive an analytical approximation of the torque using a "charge tensor" and parameterization of the target center of mass location. The AFMs and the empirical approach in Eq. (8) agree that the torque representation throughout a single-axis revolution, θ, is that in Figure 5 for a cylinder length of 3 meters. Clearly

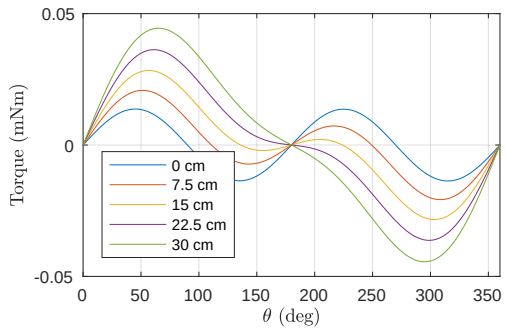

Figure 5. 3 sphere MSM cylinder torque variations for mass center offsets.[17]

visible in Figure 5 is the torque changes sign at different rotation angle values. This suggests that center-of-mass offset uncertainty may drive the detumble controller to inject momentum rather than reduce momentum for particular attitudes. This requires either strict *a priori* knowledge or an estimation scheme to obtain the true mass center to ensure constructive control. The presented analytical model in Eq. 8 is obtained by assuming an MSM distribution. The AFM formulation also includes several reducing assumptions to allow for a tractable form.[17] Therefore, modeling torque analytically is not necessarily an appealing choice for all target geometries. Required is an alternative approach to obtaining the expected torque for a commanded potential. Conveniently, the MSM distribution for a target maps the electrostatic potential to an output torque.

3.2. Lyapunov Optimal Detumble Control for Generic Geometries

The generic target detumble scheme employs an MSM distribution to compute the expected torque rather than an analytical approximation. The volume MSM distribution is most attractive for this application as it requires the fewest number of spheres to capture the electrostatic force and torque behavior. The reduced number of spheres translates to reduced computational load on a flight software system. Consider the more generic target Lyapuov function in Eq. (9) where $\boldsymbol{\omega}$ is the body angular velocity vector and I is the body-fixed inertia.

$$V = \frac{1}{2}\boldsymbol{\omega}^T I \boldsymbol{\omega} \tag{9}$$

Taking one time derivative of Eq. 9 and inserting Euler's rotational equations of motion produces the result in Eq. 10.

$$\dot{V} = \boldsymbol{\omega}^T \boldsymbol{L} \tag{10}$$

The simplicity of the Lyapunov derivative in Eq. (10) is made possible by neglecting the relative orbit motion thus assuming that the relative tumble is equal to body angular velocities. This is a reasonable assumption for significant portions of the detumble mission as is seen for the on-orbit detumble of the cylindrical target. To achieve Lyapunov optimal control, the commanded servicer potential assumes the value

$$\begin{aligned} \phi_{\text{cmd}} &= C_\phi \times \{\text{sign}(\phi) : \boldsymbol{\omega}^T \boldsymbol{L}(\phi) \leq 0\} \\ &\text{where} \quad C_\phi > 0 \end{aligned} \tag{11}$$

The control law in Eq. (11) is Lyapunov optimal and guarantees, with perfect knowledge, that the servicer will detumble the target. Setting the coefficient C_ϕ to $\phi_{\max}$ provides a bang-bang type control. The leading coefficient may be scaled based on the angular velocity to emulate the tangent saturation controller so long as the coefficient is always non-zero positive.

The Lyapunov optimal control for generic geometries does rely on the center-of-mass and inertia matrix properties. Although not as clear, the deep-space axisymmetric control also assumes perfect knowledge of these parameters. However, formulating the generic detumble control law as Lyapunov optimal using the MSM distribution allows for more clever inertia-free, or less mass-sensitive, Lyapunov functions to be applied. The formulation in Eq. (11) is a deep-space control law as it neglects the effect of relative motion on relative attitude rates. The following section applies this deep-space control law to on-orbit simulations. Additional research opportunities exist in incorporating the relative motion into the detumble Lyapunov function, however the return is minimal given that a tumble rate on the order of the orbital mean motion is sufficiently low to enable other servicer interface approaches.

3.3. Generic Target Detumble with Relative Orbit Improvements

The Lyapunov optimal control is applied to two on-orbit detumble numerical simulations to illustrate the effectiveness of the approach and improvements achieved through

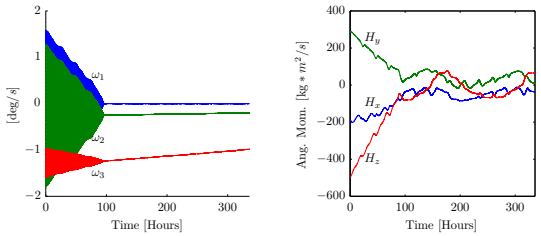

(a) Angular Velocities, Optimal (b) Inertial H_i, Optimal

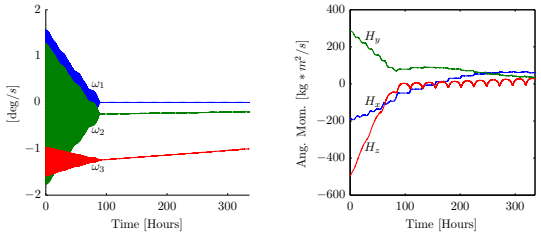

(c) Angular Velocities, Lead-Follower (d) Inertial H_i, Lead-Follower

Figure 6. Angular momentum and velocities with initial conditions: $\boldsymbol{\omega} = [-1.374,\ 0.5,\ 1.374]^\circ/sec$, comparing optimized (top row) and lead-follower (bottom row).

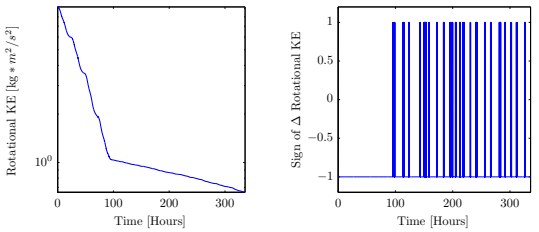

(a) Rotational Kinetic Energy, Optimal (b) Change in Rot. Kin. Energy, Optimal

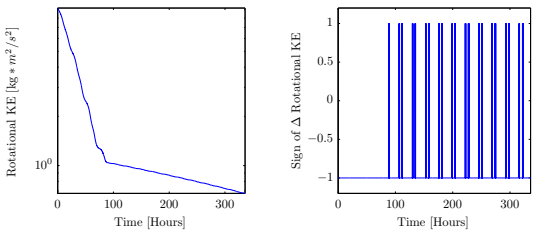

(c) Rotational Kinetic Energy, Lead-Follower (d) Change in Rot. Kin. Energy, Lead-Follower

Figure 7. Rotational kinetic energy with initial conditions: $\boldsymbol{\omega} = [0.9,\ 1.7,\ -0.6]^\circ/sec$, comparing optimized (top row) and lead-follower (bottom row).

relative orbit design. The GOES-R analogue is used as the generic target electrostatic detumble demonstrator. Similar to the axisymmetric target detumble numerical simulations, two initial conditions sets are used to illustrate the advantages of leader-follower and optimized relative orbits for shallow and steep momentum cones.[5] Choosing either the lead-follower or circularly-projected relative orbit is based on the initial momentum, applying to generic geometries as is done with axisymmetric targets.

The first example in Figure 6 is a moderate momentum cone where the tumble about the body axes is given by $\boldsymbol{\omega} = [-1.374,\ 0.5,\ 1.374]^\circ/\text{sec}$. This represents the transition point where the momentum cone is between the optimized shallow cone and the lead-follower steep cone. Recall that the box-and-panel spacecraft body frame has the z-axis aligned with the long axis of the panel, the x-axis normal to the top face of the solar panel, and the y-axis completing a right-handed system.

As can be seen in both the optimized relative trajectory and the lead-follower trajectory in Figure 6 is a rapid reduction of the angular velocity coupling between the body-fixed axes. After the 120-hour mark where the angular velocity of the first body axis is removed, the electrostatic detumble control is much less effective in removing angular momentum. Coupling between the body-fixed axes is present when all body-axis angular velocities are instantaneously non-zero. With the x-axis angular velocity as zero following the 120-hour mark, the torques perpendicular to the current angular momentum vector do not couple into detumble torques. Instead, the damped cyclic behavior that is exhibited in the post-coupling detumble demonstrates that most of the control effort is driving a re-orientation rather than reduction of the angular momentum vector. The coupling benefit is more dramatic the spherical servicer is only able to exert torque along an axis perpendicular to the relative position vector and perpendicular to the center of mass to MSM sphere vector. The limited control authority is therefore best applied against a coupled tumble where a greater percentage of the actuation torque reduces angular momentum. Comparison of the two relative orbits, Figure 6, and the change in rotational kinetic energy, Figure 7, reveals that there is no distinct advantage between these two options.

The angular velocity continues to reduce in Figures 6(a) and 6(c) as expected with the continuous Lyapunov optimal control. The dramatic change after the angular velocity coupling is eliminated is more clearly seen in the rotational kinetic energy time histories in Figure 7. The clear transition point shows that the control is less effective without the coupling. Additionally, as the angular velocity is further reduced, there are increasing sign errors due to relative motion where injection of rotational kinetic energy occurs. A second example in Figure 8 is a flat momentum cone where the tumble about the body axes is given by $\boldsymbol{\omega} = [0.9,\ 1.7,\ -0.6]^\circ/\text{sec}$. Here, the optimized relative orbit is much more suited to removing angular momentum and thus does not experience much of the cyclic behavior seen in Figure 6

The detumble benefits of coupled angular velocities are apparent when comparing the simulated cases, Figure 6 and 8. As is the case with the ω_1 coupling for the axisymmetric target, the detumble while coupled is much more effective. A point of interest with the more generic

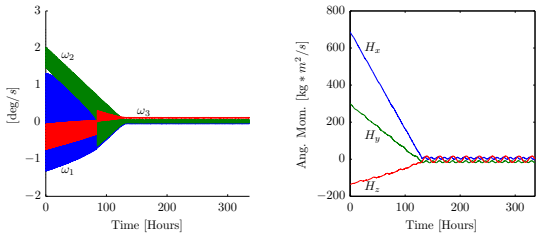

(a) Angular Velocities, Optimal (b) Inertial H_i, Optimal

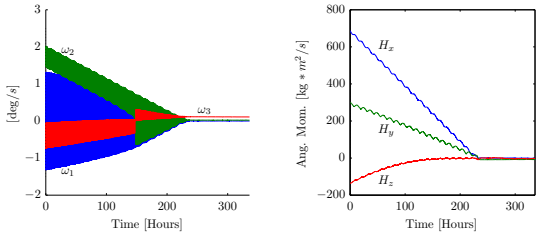

(c) Angular Velocities, Lead-Follower (d) Inertial H_i, Lead-Follower

Figure 8. Angular momentum and velocities with initial conditions: $\boldsymbol{\omega} = [0.9,\ 1.7,\ -0.6]^\circ/sec$, comparing optimized (top row) and lead-follower (bottom row).

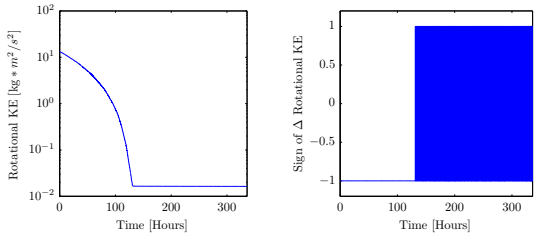

(a) Rotational Kinetic Energy, Optimal (b) Change in Rot. Kin. Energy, Optimal

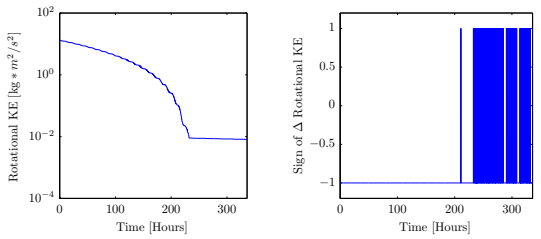

(c) Rotational Kinetic Energy, Lead-Follower (d) Change in Rot. Kin. Energy, Lead-Follower

Figure 9. Rotational kinetic energy with initial conditions: $\boldsymbol{\omega} = [0.9,\ 1.7,\ -0.6]^\circ/sec$, comparing optimized (top row) and lead-follower (bottom row).

geometry is the angular velocity change following when ω_2 first achieves zero. The improved relative geometry of the optimized orbit provides sufficient control authority to rapidly collapse the angular velocity during the entire primary detumble phase. However, the lead-follower trajectory suffers from an attitude inversion that flips the sign of ω_3. However, both cases sufficiently reduce the angular velocity. The rotational kinetic energy for the two trajectories is compared in Figure 9.

The two simulated cases provide insight into implementing on-orbit electrostatic detumble of the more generic box-and-panel spacecraft. The simulated cases clearly demonstrate the value of angular velocity coupling for electrostatic detumble. As is the case with the axisymmetric target, the best performing relative orbit is selected based on the momentum cone angle.

3.4. Minimum Multi-Sphere Model Distributions for Control

A well tuned Multi-Sphere Method target model effectively predicts control forces and torques on the target. In the interest of reducing control computational effort, this work explores reducing the target sphere distribution target models. Prior work in Reference 9 shows that a reduced 2-sphere cylinder target appropriately captures the force and torque magnitude and sign. This work extends this concept to more generic spacecraft geometries by addressing whether a reduced number of spheres used in the control formulation is sufficient for the control implementation in Eq. (11). The numerical simulation retains the full MSM model for propagating the dynamics and the output control and detumble performance are compared to the results presented in Figure 8.

The box-and-panel spacecraft provides an excellent case study because it is not axisymmetric and the center of mass and center of geometry are not coincident. The following simulations initialize the box-and-panel tumbling with angular velocities of $\boldsymbol{\omega} = [0.9,\ 1.7,\ -0.6]^\circ/\text{sec}$ and the optimized servicer LROE trajectory. This analysis seeks to address the limitations on reducing the number of spheres in the control formulation. Two additional box-and-panel MSM distributions are considered: the 2-sphere and the single sphere, or effective sphere. The center-of-mass and MSM distributions are tabulated in Table 3 where the z-axis aligned with the long axis of the panel, the x-axis normal to the top face of the solar panel, and the y-axis completing a right-handed system. Table 3 highlights some key aspects of each distribution. Inspection of the center-of-mass relative to the sphere distributions reveals that the 3-sphere and 2-sphere distributions have spheres on either side of the mass center. This is not the case with the single sphere distribution that has only one sphere on the panel-side of the mass center. The effects of these distributions are evident in the following simulations. Consider first a comparison between the 3-sphere and 2-sphere box-and-panel control formulation where the truth MSM model is 3-spheres. The resulting electrostatic detumble angular velocities and angular momentum reductions are shown in Figure 10.

The time histories in Figure 10 do not display significant differences in detumble performance during the primary detumble phase. To more clearly highlight the differences between these two control formulations, presented in Fig-

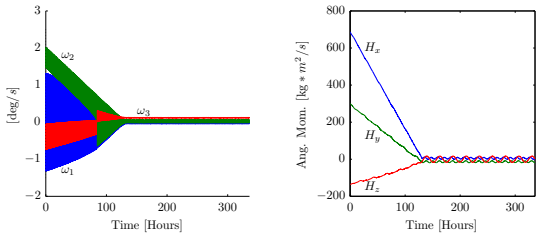

(a) Angular Velocities, Three Sphere (b) Inertial H_i, Three Sphere

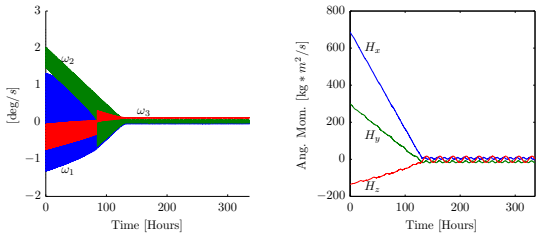

(c) Angular Velocities, Two Sphere (d) Inertial H_i, Two Sphere

Figure 10. Angular momentum and velocities with initial conditions: $\boldsymbol{\omega} = [0.9,\ 1.7,\ -0.6]^\circ/sec$, comparing both three sphere (top row) and two sphere (bottom row).

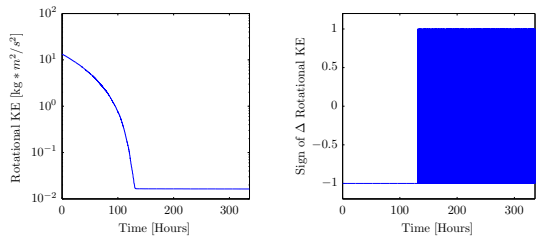

(a) Rotational Kinetic Energy, Optimal (b) Change in Rot. Kin. Energy, Optimal

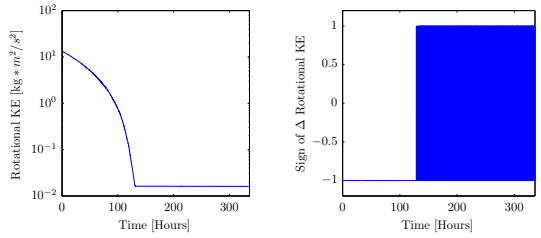

(c) Rotational Kinetic Energy, Lead-Follower (d) Change in Rot. Kin. Energy, Lead-Follower

Figure 11. Rotational kinetic energy with initial conditions: $\boldsymbol{\omega} = [0.9,\ 1.7,\ -0.6]^\circ/sec$, comparing 3-sphere (top row) and 2-sphere (bottom row) targets.

ure 11 are the semi-logarithmic rotational kinetic energy time histories paired with the sign of the change in rotational kinetic energy from the previous time step.

The immediately noticeable difference between the two formulations is the continual detumble of the 3-sphere

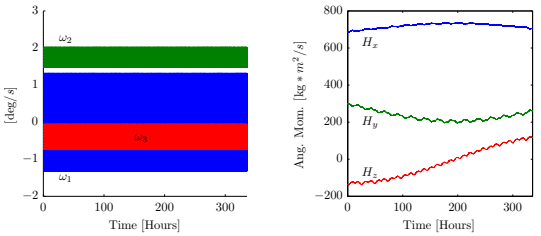

(a) Angular Velocities, Three Sphere (b) Inertial H_i, Three Sphere

Figure 12. Angular momentum and velocities with initial conditions: $\boldsymbol{\omega} = [0.9,\ 1.7,\ -0.6]^\circ/sec$, one sphere target.

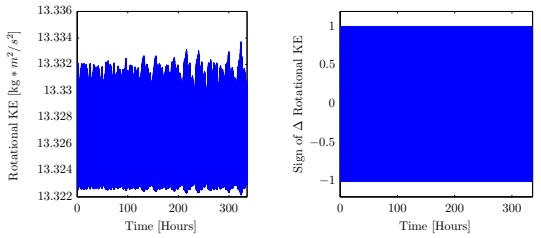

(a) Rotational Kinetic Energy, Lead-Follower (b) Change in Rot. Kin. Energy, Lead-Follower

Figure 13. Rotational kinetic energy with initial conditions: $\boldsymbol{\omega} = [0.9,\ 1.7,\ -0.6]^\circ/sec$, one sphere target.

distribution. Both the 3-sphere and 2-sphere models are plagued by neglecting the relative orbit contribution to relative attitude rate; however, the 3-sphere model has the same truth and control formulation and is therefore able to more accurately capture the torque. This reasonable agreement between the 3-sphere and 2-sphere control formulations motivates further reduction to a single, or effective, sphere model. The detumble results of the single sphere control implementation are shown in Figure 12.

The angular momentum behavior in Figure 12(b) appears to be cyclic in nature where the electrostatic actuation is merely precessing the inertial angular momentum vector rather than imparting any significant increase or decrease in magnitude. The single sphere case does not properly capture the simple switching because it is biased to one side of the center of mass. That is, the control predicts the incorrect torque direction for particular attitudes. This is further supported by the continual insertion and extraction of rotational kinetic energy: Figure 13. Clearly in Figure 13(b), the kinetic energy contribution is dependent on the particular attitude as the target rotates and thus switches signs on the order of half a rotation period.

These results suggest that a suitable MSM model used for control torque evaluations must have at least on sphere on opposing sides of the center of mass (center of rotation) for each axis with an offset dictating that two is the minimum number of spheres for any detumble con-

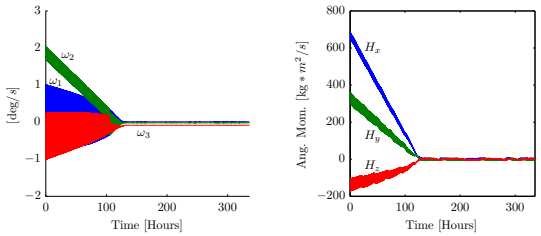

(a) Angular Velocities, Mass Offset (b) Inertial H_i, Mass Offset

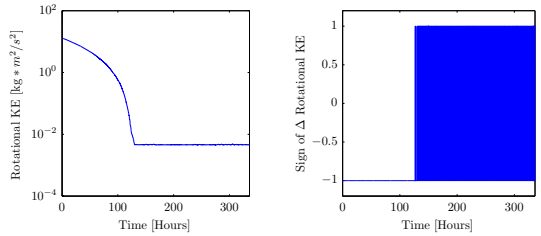

(c) Rotational Kinetic Energy, Mass Offset (d) Change in Rot. Kin. Energy, Mass Offset

Figure 14. Rotational kinetic energy with initial conditions $\boldsymbol{\omega} = [0.9,\ 1.7,\ -0.6]^\circ/sec$ when the offset mass is moved along the positive x-axis.

trol MSM formulation. Inspection of the 2-sphere box-and-panel distribution reveals that the spheres straddle the mass center in both the y and z axes. This suggests that the 2-sphere, and even 3-sphere,[36] cylinder model in Reference 9 where the spheres are along the slender axis would only be valid for mass center offsets along the slender axis and no other axis. Therefore, a valid control MSM model requires a sphere pair to straddle the mass center for every axis where a mass offset exists.

3.5. Additional Investigation of Mass Offset for MSM Distributions

The assertion that the mass center must be bounded by electrostatic spheres is further investigated using the 3-sphere box-and-panel distribution. Recall that in Table 2 that an offset mass of 1000 kg could be moved to an offset location of $[1.5,\ 0.0,\ 0.0]$ meters from the bus center yielding a new mass center location of $[0.5,\ 0.238,\ 0.9775]$ meters. The current 3-sphere distribution only places spheres in the y-z geometrical symmetry plane and therefore does not bound the new mass center location. The detumble results of the box-and-panel with a mass center offset are shown in Figure 14.

The addition of mass offset along the body x-axis does develop into a fully populated inertia matrix. However, the x-axis is the intermediate axis of inertia and the x and y axes have inertias 5 times that of the z-axis where the spheres are located in the $y4$-z plane of the spacecraft. The coupling present from an x mass offset provides incorrect torque sign about this axis because the spheres do not bound the mass center. Current results suggest that the elongated sphere distribution used for the box-and-panel spacecraft does not amplify the errors in an x offset center-of-mass location. The torque does have the incorrect sign about either the y or $z$axes with an x axis mass offset, however the dominant torque is about the x and z axes recalling z has the smallest inertia. The presented box-and-panel geometry and admissible offsets in the body x-axis does not clearly challenge nor support the assertion that spheres must bound the mass center.

Consistent with previous analysis, the body axis rotation rate coupling introduced by a a full inertia matrix produces more complete detumble. Comparison of Figure **??** to Figure 9(a) shows that the mass offset contribution enables half an order of magnitude more complete detumble. This is in part due to the fixed relative orbit of the servicer. The body axis coupling supplants some degradation in controllability for reduced tumble rates. The primary detumble phase for the mass offset and other examples are made more complete if the servicer reconfigures the relative orbit throughout the detumble or at key opportunities. However, the full body axis coupling may render relative orbit reconfiguration less necessary.

4. CONCLUSIONS

Numerical simulations demonstrate that a Lyapunov optimal control approach is viable for generic target geometries. The most effective detumble control for a spherical servicer is present when angular velocity coupling is present on the target craft. Also of importance is the demonstration that the Multi-Sphere model of the target craft does not need to be the highest-fidelity model to accurately control the commanded servicer potential. The requirement that sphere pairs straddle the center-of-mass on any mass offset axis remains the only known limitation on a reduced MSM distribution. This supports that the on-board system may be able to use small-number Multi-Sphere models in control formulations.

This work further investigates the axisymmetric cylinder electrostatic detumble performance with a time-varying relative position controlled by the developed Linearized Relative Orbit Elements (LROEs) formulation. Given the optimization sweep over the angular momentum cone space, the lead-follower is used for any formation that has an angular momentum cone angle less than about 30-40 degrees where the optimized LROE state is used otherwise. As shown by the numerical simulations, the use of relative motion enables near-complete detumble of 2°/sec target tumble in as little as 5 operation days. The lead-follower relative orbit provides sufficient detumble performance for limited relative orbit complexity where the optimized relative orbit provides a reduction of days in detumble operation time for some cases. The on-orbit relative motion optimization is valid for any spacecraft geometry and only requires knowledge of the initial, or current, angular momentum vector.

5. ACKNOWLEDGEMENTS

The authors would like to thank the NASA Space Technology Research Fellowship (NSTRF) program, grant number NNX14AL62H, for support of this research.

REFERENCES

1. Paul V. Anderson and Hanspeter Schaub. Methodology for characterizing high-risk orbital debris in the geosynchronous orbit regime. In *AAS/AIAA Space Flight Mechanics Meeting*, Williamsburg, VA, Jan. 11–15 2015. Paper AAS 15-204.

2. Antonella A. Albuja, Daniel J. Scheeres, and Jay W. McMahon. Evolution of angular velocity for defunct satellites as a result of yorp: An initial study. *Advances in Space Research*, 56(2):237–251, July 2015.

3. John Berryman and Hanspeter Schaub. Analytical charge analysis for 2- and 3-craft coulomb formations. *AIAA Journal of Guidance, Control, and Dynamics*, 30(6):1701–1710, Nov.–Dec. 2007.

4. Trevor Bennett and Hanspeter Schaub. Touchless electrostatic detumbling while tugging large axi-symmetric geo debris. In *25th AAS/AIAA Spaceflight Mechanics Meeting*, Williamsburg, Virginia, Jan. 11–15 2015. Paper AAS 15-383.

5. Trevor Bennett and Hanspeter Schaub. Capitalizing on relative motion in electrostatic detumbling of axi-symmetric geo objects. In *6th International Conference on Astrodynamics Tools and Techniques (ICATT)*, Darmstadt, Germany, March 14–17 2016.

6. Trevor Bennett and Hanspeter Schaub. Continuous-time modeling and control using nonsingular linearized relative-orbit elements. *Journal of Guidance, Control, and Dynamics*, pages 1–10, 2016/10/24 2016.

7. Trevor Bennett, Daan Stevenson, Erik Hogan, Lauren McManus, and Hanspeter Schaub. Prospects and challenges of touchless debris despinning using electrostatics. *Advances in Space Research*, 56(3):557–568, Aug. 2015.

8. Eleonora M. Botta, Inna Sharf, and Arun Misra. Tether-nets for active space debris removal: Effect of the tether on deployment and capture dynamics. In *27th AAS/AIAA Space Flight Mechanics Meeting*, San Antonio, TX, February 5-9 2017.

9. Philip Chow, Joseph Hughes, Trevor Bennett, and Hanspeter Schaub. Automated sphere geometry optimization for the volume multi-sphere method. In *AAS/AIAA Spaceflight Mechanics Meeting*, Napa Valley, California, Feb. 14–18 2016. Paper No. AAS-16-472.

10. John H. Cover, Wolfgang Knauer, and Hans A. Maurer. Lightweight reflecting structures utilizing electrostatic inflation. US Patent 3,546,706, October 1966.

11. Philip Chrystal, Darren McKnight, Pamela L. Meredith, Jan Schmidt, Marcel Fok, and Charles Wetton. Space debris: On collision course for insurers? Technical report, Swiss Reinsurance Company Ltd, Zürich, Switzerland, March 2011.

12. Patrice Couzin, Frank Teti, and R. Rembala. Active removal of large debris: System approach of deorbiting concepts and technological issues. In *6th European Conference on Space Debris*, Darmstadt, Germany, April 22–25 2013. Paper No. 6a.P-17.

13. W. H. Clohessy and R. S. Wiltshire. Terminal guidance system for satellite rendezvous. *Journal of the Aerospace Sciences*, 27(9):653–658, Sept. 1960.

14. Rao Surampudi et. al. Solar cell and array technology for future space missions. Technical Report D-24454, National Aeronautics and Space Administration, June 2002.

15. Erik Hogan and Hanspeter Schaub. Space debris reorbiting using electrostatic actuation. In *AAS Guidance and Control Conference*, Breckenridge, CO, Feb. 3–8 2012. Paper AAS 12–016.

16. Erik Hogan and Hanspeter Schaub. Relative motion control for two-spacecraft electrostatic orbit corrections. *AIAA Journal of Guidance, Control, and Dynamics*, 36(1):240–249, Jan. – Feb. 2013.

17. Joseph Hughes and Hanspeter Schaub. Spacecraft electrostatic force and torque expansions yielding appropriate fidelity measures. In *AAS Spaceflight Mechanics Meeting*, San Antonio, TX, Feb. 5–9 2017. Paper AAS 17–441.

18. Gabriel Ingram, Joseph Hughes, Trevor Bennett, Christine Hartzell, and Hanspeter Schaub. Autonomous volume multi-sphere-model development using electric field matching. In *AAS Spaceflight Mechanics Meeting*, San Antonio, TX, Feb. 5–9 2017. Paper AAS 17-451.

19. Yu S. Karavaev, R. M Kopyatkevich, M. N. Mishina, G. S. Mishin, P. G. Papushev, and P. N. Shaburov. The dynamic properties of rotation and optical characteristics of space debris at geostationary orbit. In *Advances in the Astronautical Sciences*, volume 119, pages 1457–1466, 2004. Paper No. AAS-04-192.

20. Lyon B. King, Gordon G. Parker, Satwik Deshmukh, and Jer-Hong Chong. Spacecraft formation-flying using inter-vehicle coulomb forces. Technical report, NASA/NIAC, January 2002. `http://www.niac.usra.edu`.

21. Naomi Murdoch, Dario Izzo, Claudio Bombardelli, Ian Carnelli, Alain Hilgers, and David Rodgers. The electrostatic tractor for asteroid deflection. In *58th International Astronautical Congress*, 2008. Paper IAC-08-A3.I.5.

22. Naomi Murdoch, Dario Izzo, Claudio Bombardelli, Ian Carnelli, Alain Hilgers, and David Rodgers. Electrostatic tractor for near earth object deflection. In *59th International Astronautical Congress*, Glasgow Scotland, 2008. Paper IAC-08-A3.I.5.

23. Daniel F. Moorer and Hanspeter Schaub. Electrostatic spacecraft reorbiter. US Patent 8,205,838 B2, Feb. 17 2011.

24. Daniel F. Moorer and Hanspeter Schaub. Hybrid electrostatic space tug. US Patent 0036951-A1, Feb. 17 2011.

25. Andrew Ogilvie, Justin Allport, Michael Hannah, and John Lymer. Autonomous satellite servicing using the orbital express demonstration manipulator system. In *Proc. of the 9th International Symposium on Artificial Intelligence, Robotics and Automation in Space (i-SAIRAS'08)*, pages 25–29, Hollywood, CA, February 26-29 2008.

26. Mason A. Peck. Prospects and challenges for lorentz-augmented orbits. In *AIAA Guidance, Navigation and Control Conference*, San Francisco, CA, August 15–18 2005. Paper No. AIAA 2005-5995.

27. J. Reed, J. Busquets, and C. White. Grappling system for capturing heavy space debris. In *2nd European Workshop on Active Debris Removal*, Paris, France, 2012. Paper 4.2.

28. J. Starke, B. Bischof, W. H. Foth, and H. J. Guenther. Roger, a potential orbital space debris removal system. In *NASA/DARPA International Conference on Orbital Debris Removal*, Chantilly VA, December 8-10 2009.

29. Josip Sliško and Raúl A. Brito-Orta. On approximate formulas for the electrostatic force between two conducting spheres. *American Journal of Physics*, 66(4):352–355, 1998.

30. Hanspeter Schaub and John L. Junkins. *Analytical Mechanics of Space Systems*. AIAA Education Series, Reston, VA, 2nd edition, October 2009.

31. Hanspeter Schaub and Daniel F. Moorer. Geosynchronous large debris reorbiter: Challenges and prospects. In *AAS Kyle T. Alfriend Astrodynamics Symposium*, Monterey, CA, May 17–19 2010. Paper No. AAS 10-311.

32. W. R. Smythe. *Static and Dynamic Electricity*. McGraw–Hill, 3rd edition, 1968.

33. Brett Streetman and Mason A. Peck. New synchronous orbits using the geomagentic lorentz force. *AIAA Journal of Guidance, Control, and Dynamics*, 30(6):1677–1690, Nov.–Dec. 2007.

34. Carl R. Seubert, Stephan Panosian, and Hanspeter Schaub. Analysis of a tethered coulomb structure applied to close proximity situational awareness. *AIAA Journal of Spacecraft and Rockets*, 49(6):1183–1193, Nov. – Dec. 2012.

35. Hanspeter Schaub and Daan Stevenson. Prospects of relative attitude control using coulomb actuation. In *Jer-Nan Juang Astrodynamics Symposium*, College Station, TX, June 25–26 2012. Paper AAS 12–607.

36. Daan Stevenson and Hanspeter Schaub. Multi-sphere method for modeling electrostatic forces and torques. *Advances in Space Research*, 51(1):10–20, Jan. 2013.

37. Daan Stevenson and Hanspeter Schaub. Rotational testbed for coulomb induced spacecraft attitude control. In *5th International Conference on Spacecraft Formation Flying Missions and Technologies*, Münich, Germany, May 29–31 2013.

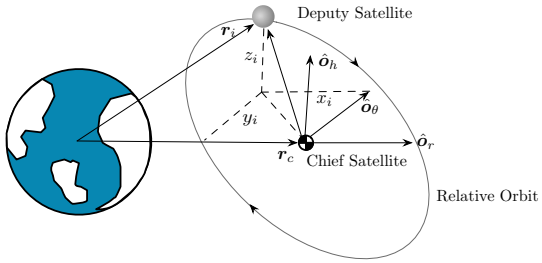

Figure 15. Local vertical local horizontal rotating Hill frame.[30]

38. Laura A. Stiles, Hanspeter Schaub, Kurt K. Maute, and Daniel F. Moorer. Electrostatically inflated gossamer space structure voltage requirements due to orbital perturbations. *Acta Astronautica*, 84:109–121, Mar.–Apr. 2013.

39. Shuquan Wang and Hanspeter Schaub. Nonlinear charge control for a collinear fixed shape three-craft equilibrium. *AIAA Journal of Guidance, Control, and Dynamics*, 34(2):359–366, Mar.–Apr. 2011.

40. Wenfu Xu, Bin Liang, Bing Li, and Yangsheng Xu. A universal on-orbit servicing system used in the geostationary orbit. *Advances in Space Research*, 48(1):95–119, 2011.

A. GUIDANCE AND CONTROL USING LINEARIZED RELATIVE ORBIT ELEMENTS

Motivated are relative orbits that capitalize on the natural relative motion of orbiting formations to improve the detumble performance. Considered by this study are detumble targets in the Geostationary (GEO) orbit regime which is a prime candidate for applying the Clohessy-Wiltshire (CW) relative orbit equations.[13] The relative motion of the considered ROEs are derived in the Hill frame defined in Figure 15. The Hill frame is defined by $\mathcal{H} = \{\hat{\boldsymbol{o}}_r, \hat{\boldsymbol{o}}_\theta, \hat{\boldsymbol{o}}_h\}$ where $\hat{\boldsymbol{o}}_r$ is aligned with the reference craft orbit radius, $\hat{\boldsymbol{o}}_h$ is aligned with the reference craft orbit angular momentum, and $\hat{\boldsymbol{o}}_\theta$ completes the orthonormal reference frame. The deputy spacecraft motion is described relative to a chief reference craft. The focus of this work is the reduction of the relative orbit problem to the Clohessy-Wiltshire (CW) equations that describe the motion of the deputy about a circular reference orbit. While the CW equations provide a suitable relative position description, the newly developed guidance and control methodology using the CW integration constants is utilized.[6] A slight modification to the CW equations removes the ambiguity when α and β are zero through trigonometric expansion and largely preserves the inherent insight. The modified non-singular CW equations are

$$x(t) = A_1 \cos(nt) - A_2 \sin(nt) + x_{\text{off}} \tag{12a}$$

$$y(t) = -2A_1 \sin(nt) - 2A_2 \cos(nt) - \frac{3}{2} nt x_{\text{off}} + y_{\text{off}} \tag{12b}$$

$$z(t) = B_1 \cos(nt) - B_2 \sin(nt) \tag{12c}$$

The state vector for Linearized Relative Orbit Element (LROE) guidance is the collection of the CW equations' integration constants not the Cartesian state. The LROE form provides the relative motion geometry in the absence of perturbations where these parameters remain constant. The nominally invariant nonsingular LROE state vector $\boldsymbol{X}_{\text{NS}}$, defined as

$$\boldsymbol{X} = [A_1, A_2, x_{\text{off}}, y_{\text{off}}, B_1, B_2] \tag{13}$$

First derived in Reference,[6] the dynamics of the LROE state in the presence of perturbations can be obtained by applying Lagrange Brackets to the non-singular LROE equations. This approach is analogous to Lagrange's planetary equations in that the LROE set becomes osculating to match the perturbed relative orbit. The nonsingular state vector in (13) evolves according to (14) where $\boldsymbol{a}_d$ is the disturbance acceleration in the Hill frame.[6]

$$\dot{\boldsymbol{X}} = \underbrace{\frac{1}{n} \begin{bmatrix} -\sin(nt) & -2\cos(nt) & 0 \\ -\cos(nt) & 2\sin(nt) & 0 \\ 0 & 2 & 0 \\ -2 & 3nt & 0 \\ 0 & 0 & -\sin(nt) \\ 0 & 0 & -\cos(nt) \end{bmatrix}}_{B(\boldsymbol{X},t)} \begin{bmatrix} a_x \\ a_y \\ a_z \end{bmatrix} \tag{14}$$

Given that the LROE state evolves from perturbation accelerations, a Psuedo-Inverse relative motion controller is applied to achieve the desired relative orbit by injecting a control acceleration into (14). The LROE state error can be defined as

$$\Delta\text{œ} = \boldsymbol{X} - \boldsymbol{X}_r \tag{15a}$$

$$\Delta\dot{\text{œ}} = \dot{\boldsymbol{X}} - \dot{\boldsymbol{X}}_r = [B](\boldsymbol{u} - \boldsymbol{u}_r) \tag{15b}$$

where the $()_r$ denotes the reference trajectory. The time rate of the LROE error measure also allows the reference trajectory to be defined by a LROE rate. Shown in Reference,[6] the Lyapunov asymptotically-stable feedback control law is

$$\boldsymbol{u} = -([B]^T[B])^{-1}[B]^T[K]\Delta\text{œ} \tag{16}$$

The simple feedback form allows the implemented control to apply a corrective acceleration to maintain the desired relative orbit in the presence of perturbations. Consider the effect of the electrostatic force during proximity electrostatic interaction between the servicer as the deputy object with the target cylinder at the origin of the Hill coordinate frame. The attractive and repulsive forces on the servicer will perturb the relative orbit of the servicer about the target object. The current study utilizes the control form in (16) to maintain the desired relative orbit in the presence of electrostatic forces. In addition, the guidance control enables feed-forward of perturbation accelerations. For example, the electrostatic force acting on the servicer may be predicted using MSM and fed forward to the controller as part of the corrective maneuvering.

The gain developed for the LROE controller is set to provide a bounding box of 1% of the relative separation distance. The gain is scaled by the mean motion of the chief orbit such that the relative motion leverages the natural dynamics of formation flying.

$$[K] = (n \cdot 10^4) \times \text{diag}([1,\ 1,\ 30,\ 1,\ 1,\ 1]) \tag{17}$$

The gain matrix utilized may not be optimal, however sufficient performance is obtained. Future studies will address the gain matrix and seek dynamical system leverage in precisely scaling the gain values.

The LROE orbit optimization approach leverages MATLAB's *fmincon* optimizer. While many optimization toolboxes exist, *fmincon* provides the state bounds, simplicity of implementation, and wealth of documentation to provide a sufficient first analysis of the desired approach. The following optimization approach requires a robustness addition because MATLAB's *fmincon* optimizer does not guarantee a global minimum. The utilized optimization cost function that minimizes both the separation distance and minimizes the off-perpendicular alignment of the relative position and momentum vector. First considered is a cost function that utilizes just the torque obtained for the particular relative position and attitudes about the angular momentum vector. However, this approach introduces local minima because the cost function relies on a sweep of attitudes and additional discretization assumptions. Therefore, a more general cost function that does not require instantaneous attitude information is leveraged to help reduce the number of local minima.[5] The relative orbit elements are selected as the optimization state variables because these elements are directly sensed and controlled by the servicer spacecraft. Any optimization over the detumbling time and fuel usage requires multi-day GEO simulations at small time scales and thus large computational effort. However the detumbling time is directly proportional to the relative orbit configuration and inversely proportional to the separation distance. Thus, a cost function that maximizes the geometrical detumble torque opportunity and minimizes the separation distance achieves reductions in detumble time. The inclusion of relative position in the cost function allows the optimizer to trade significant improvements in geometry for separation distance.[5]

$$\begin{aligned} J = \sum_{i=0}^{N} (&-1000 \ln[|\boldsymbol{r}_i| - r^* + 1] \\ &- 10 \ln\left[\left|\frac{\boldsymbol{r}_i \cdot \boldsymbol{H}_i}{\|\boldsymbol{r}_i\|\|\boldsymbol{H}_i\|}\right| + 1\right]) \end{aligned} \tag{18}$$

The cost in EQ. (18) is accumulated over a single discretized relative orbit with N time segments. This study

utilizes 50 uniform time segments. The relative position and angular momentum are expressed in the Hill frame where $\boldsymbol{r}_i = \boldsymbol{r}(t_i)$ and $\boldsymbol{H}_i = \boldsymbol{H}(t_i)$ at time t_i. The minimum separation distance is prescribed by r^*. The relative weights are selected to achieve the same order of magnitude contribution for both separation distance and angle error. Both values are increased by an order of magnitude to help the convergence characteristics of the *fmincon* optimizer. Only positive values of the LROE state are considered. This limits the relative orbit space to only the positive combinations, however it captures the full space in the cost function.